Short communication

Enhanced electrochemical performance of different morphological C/LiMnPO$_4$ nanoparticles from hollow-sphere Li$_3$PO$_4$ precursor via a delicate polyol-assisted hydrothermal method

Yu-Ting Cui [a], Ning Xu [b], Li-Qin Kou [a], Meng-Tao Wu [b], Li Chen [a,*]

[a] Department of Chemistry, Tianjin University, Tianjin 300072, People's Republic of China
[b] Tianjin B&M Science and Technology Joint-Stock Co., Ltd., Tianjin 300384, People's Republic of China

HIGHLIGHTS

- A delicate polyol-assisted hydrothermal method to synthesize LiMnPO$_4$ is present.
- Pre-synthesized hollow-sphere Li$_3$PO$_4$ particles are used as precursor.
- Influence of water–DEG ratio on the LiMnPO$_4$ morphology is investigated.
- Excellent capacity retentions indicate the weaker Jahn–Teller effect.
- The flaky shaped sample delivers 60% initial capacity (154.1 mA h g^{-1}) at 4 C rate.

ARTICLE INFO

ABSTRACT

With the hollow-sphere Li$_3$PO$_4$ as precursor, a delicate polyol-assisted hydrothermal method is devised to synthesize high-performance LiMnPO$_4$. Orthorhombic shaped, irregular flaky shaped and sphere-like LiMnPO$_4$ are sequentially prepared by decreasing the water–diethylene glycol (DEG) ratio. The capacity, cycling stability and rate performance of all samples prepared by the new synthesis method are improved significantly. And the C/LiMnPO$_4$ with irregular flaky shape exhibits a capacity of 154.1 mA h g^{-1} at C/20, 147.4 mA h g^{-1} at C/10 and 102.5 mA h g^{-1} at 2 C, which is the best performance ever reported for LiMnPO$_4$ active material with similar carbon additives.

1. Introduction

Encouraged by the successful attempts on LiFePO$_4$, LiMnPO$_4$ with a higher theoretical energy density (701 Wh kg^{-1}) than that of LiFePO$_4$ (586 Wh kg^{-1}) [1–4], has increasingly attracted attention recently. However, the application of LiMnPO$_4$ is limited by its intrinsically low ionic and electronic conductivity [5,6]. Tremendous efforts have been made to overcome these limitations, such as particle size minimization, substitution doping and improvement in interfacial contact resistance [2,4,7,8,12–15]. Because the electrochemical properties are significantly affected by the anisotropy of lithium ion intercalation/detercalation in phosphor–olivine which has a close relationship with the crystal morphology, we focus our attention on the material synthesis process to regulate the size, the agglomeration degree and the morphologies of particles to achieve the desired composite architecture.

So far, many methods have been attempted to synthesize phase-pure LiMnPO$_4$, and the promising methods among them seem to be the direct precipitation, the polyol synthesis, the hydrothermal synthesis and the spray pyrolysis method [2,7–15]. In this study, a delicate polyol-assisted hydrothermal method is put forward to synthesize high-performance LiMnPO$_4$. To suppress particle growth and agglomeration, a Li$_3$PO$_4$ precursor with hollow sphere structure is used to induce the oriented growth of LiMnPO$_4$ on its particles surface. The particle morphologies can be controlled by changing the water–DEG ratio. Primary results indicate that the new synthesis method shows great promise for improving the electrochemical performance of LiMnPO$_4$.

* Corresponding author. Tel.: +86 22 27892379; fax: +86 22 27403475.
E-mail address: chenli_su@eyou.com (L. Chen).

2. Experimental

All chemicals were purchased from Aladdin Reagent and used directly without further purification.

2.1. Preparation of LiMnPO₄

The Li_3PO_4 precursor was precipitated by dropping 1.1 mol L^{-1} H_3PO_4 (85% solution) into a 0.4 mol L^{-1} LiOH (99%) aqueous solution and the flow rate was 0.75 mL min^{-1}. The resulting white precipitates were washed with distilled water and dried in air at 120 °C. $MnSO_4 \cdot H_2O$ (99%) and the above Li_3PO_4 (at a 1:1 M ratio) were wet ball-milled in water−DEG mixed solvents for 0.5 h, then the slurry was transferred into a Teflon-lined autoclave, and heated at 190 °C for 24 h. Finally, the obtained materials were washed in sequence with anhydrous alcohol and deionized water thoroughly, and dried at 80 °C for 3 h under vacuum to get $LiMnPO_4$ powder.

2.2. Carbon-coating

The carbon coating process proceeded according to the procedure reported by Dahn et al. [3]. The $LiMnPO_4$ was mixed with a sucrose solution in a 10:3 weight ratio. After sonicated for 4 h, the water suspension was evaporated at 50 °C under vacuum. Then the dried sucrose/$LiMnPO_4$ composite was heated at 300 °C for 1 h and calcined at 600 °C for 3 h under Ar gas flow to synthesize the carbon coated $LiMnPO_4$ particles (C-LMP).

2.3. Apparatus

The samples were studied by X-ray diffraction (XRD, D/max 2500 V/PC, Rigaku, 40 KV) using Cu Kα radiation and a bent graphite monochromatic with a scan speed of 2 ° min^{-1} in the 2θ range 10−90°. Quantitative elemental analysis was carried out by inductively coupled plasma atomic emission spectroscopy (ICP-AES) with a Varian Liberty 100 instrument. The analyzed samples were dissolved in hot concentrated HCl: HNO_3 mixture at a 3:1 M ratio. A field-emission scanning electron microscope (FE-SEM, XL30, Philips) was used to investigate sample morphology. A field-emission high-resolution transmission electron microscope (FEHRTEM, JEM-2100F, JEOL) was used to observe the interior structures of samples. Electrochemical impedance spectroscopy (EIS, Zennium, Zhaner Elektrik) was carried out in the frequency range from 0.1 Hz to 100 kHz and a ±5 mV AC signal. An infrared

carbon and sulfur analyzer (CS-901B, Haotianhui) was used to analyze the carbon content of samples.

The cathode was prepared by coating a viscous slurry with 80% C-LMP composite, 10% conductive carbon black (Super P), and 10% polyvinylidene fluoride (PVDF) binder onto Al foil, then further dried at 120 °C for 3 h. The dried electrode was punched into round disks (1.2 cm in diameter, 32 μm in thickness), and each disk comprises 3 mg active material. The electrolyte was 1 M $LiPF_6$ in an ethylene carbonate (EC) and dimethyl carbonate (DEC) solution with 1:1 volume ratio. CR2032 coin cells were assembled in an argon-filled glove box with the prepared cathodes and Li anodes. The cells were tested on a CT2001A LAND battery testing system at room temperature according to the following procedure: ① charged to 4.5 V (vs. Li/Li$^+$) galvanostatically; ② charged for 1.5 h in the constant voltage mode; ③ discharge galvanostatically to 2.5 V at different rates from C/20 to 4 C. "C/n" here means the current which is used to discharge the nominal capacity in "n" hours (assuming $LiMnPO_4$ as the active material, e.g. 4 C corresponds to discharge in 1/4 h, and the current is calculated to be 170 mA h g^{-1}/ (1/4 h) = 680 mA g^{-1}).

3. Results and discussion

The molar ratio of H_2O to DEG, which is hereafter defined as $X = H_2O$ mole number/DEG mole number, is changed by adding different amounts of DEG to the reaction mixtures. When there is no DEG, the corresponding sample is named as Sample-BS.

X-ray diffraction pattern of Li_3PO_4 precursor is shown in Fig. 1a. All the diffraction peaks are in good agreement with that of standard Li_3PO_4 (PDF#25-1030). No impurity peaks are observed, which indicates the high-purity Li_3PO_4 precursor is achieved. The insets in Fig. 1a show the hollow sphere morphology of Li_3PO_4 ($\sim$400 nm in diameter) which is formed by the resolubilization−precipitation cycles between Li_2HPO_4 and Li_3PO_4 [8] during precipitation process. The sphere shell consists of primary Li_3PO_4 particles about 16 nm diameters (calculated by the Scherrer Formula). The X-ray diffraction in Fig. 1b confirms the synthesized LMP crystal is olivine structure, but Li_3PO_4 impurity phase is detected for Sample $X = 0.5$. The elemental analysis results are listed in Supplementary data (Table S1), which confirm that the stoichiometrical $LiMnPO_4$ powders can be hydrothermally prepared. The refined lattice parameters and volumes calculated by Rietveld refinement are shown in Table 1, which agree well with literature data [10,13]. The ratio of (020) and (311) changes from 0.78 in standard spectrum to 0.99 for
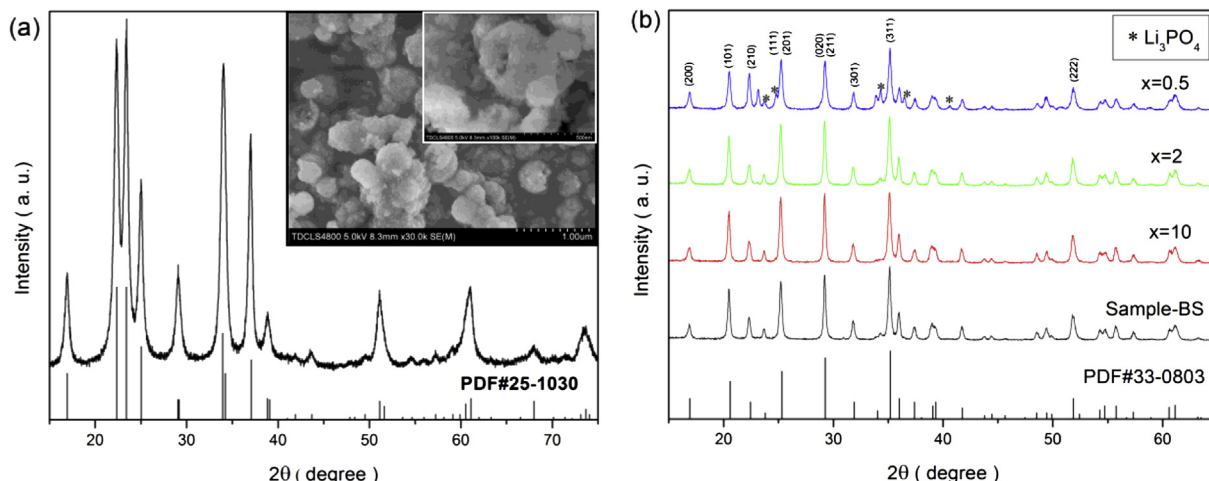

Fig. 1. XRD patterns of (a) the intermediate precipitate Li_3PO_4, inset: FE-SEM of Li_3PO_4, and (b) C-LMP samples prepared in different solvents.

Table 1
Lattice parameters, mean crystalline sizes and the ratio of I_{020}/I_{311}.

Sample	a (Å)	b (Å)	c (Å)	Volume (Å)	Particle size (nm)	I_{020}/I_{311}
$X = 0.5\ x = 0.78$	6.10740	10.4490	4.7460	302.87	29.10	0.80
$X = 2$	6.10460	10.4666	4.7456	303.22	33.46	0.99
$X = 10$	6.10660	10.4515	4.7467	302.95	37.36	0.94
Sample-BS	6.12093	10.4473	4.7439	302.47	41.20	0.79
Li_3PO_4	6.08606	10.4851	4.8601	310.18	16.20	—

$X = 2$ sample. This change indicates the flakelet preferentially orients in the $a-c$ plane [9], which leads to the formation of a shorter Li^+ diffusion pathway paralleling to the direction of flakelet thickness (b-axis orientation). The carbon contents are about 6.3 wt % according to the measurement results of the infrared carbon–sulfur analyzer, and the absence of carbon peaks in XRD patterns indicates the amorphous nature of the residual carbon pyrolyzed from the sucrose.

The FE-SEM images in Fig. 2 show the different morphologies of C-LMP powders. Multi-morphology nanoparticles of Sample-BS are observed in Fig. 2a. Orthorhombic shaped, irregular flaky shaped and sphere-liked $LiMnPO_4$ in Fig. 2b–d are prepared by changing X value from 10 to 2 and 0.5, respectively. The morphology difference can be attributed to the different crystal growing environments caused by the varying mixed solvents. The FE-SEM images of the hydrothermally prepared $LiMnPO_4$ are shown in Supplementary data (Fig. S1). By comparing the images before and after carbon coating process, we confirm that the morphologies of the $LiMnPO_4$
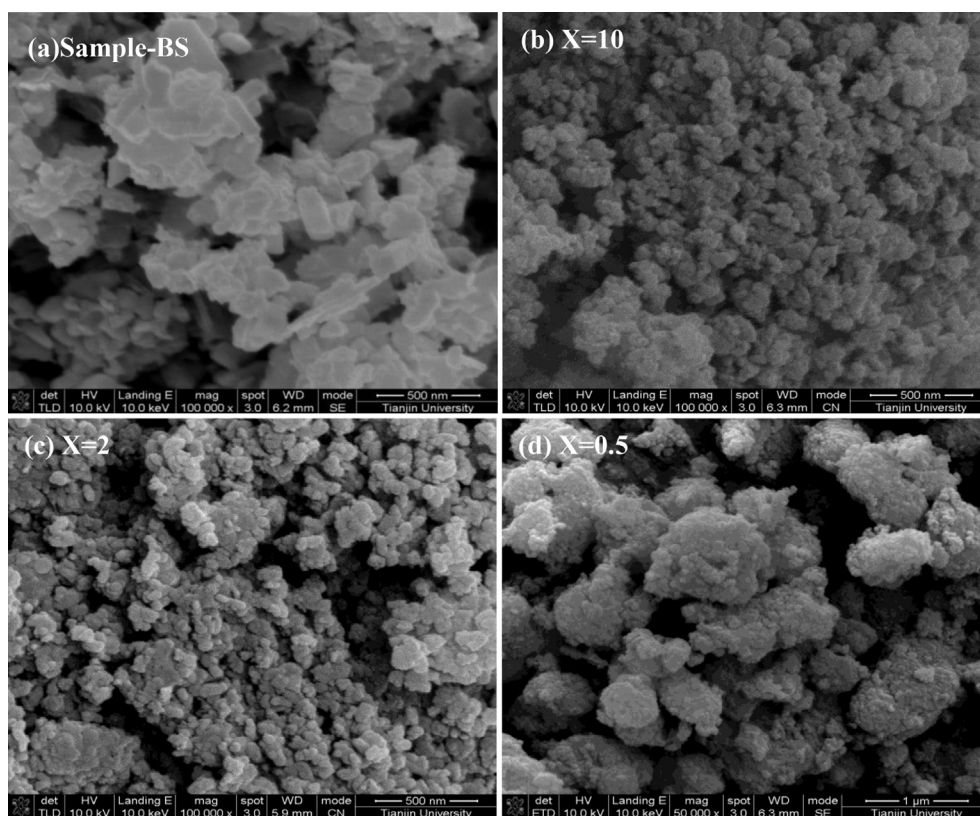

Fig. 2. (a–d) FE-SEM micrographs of C-LMP samples.
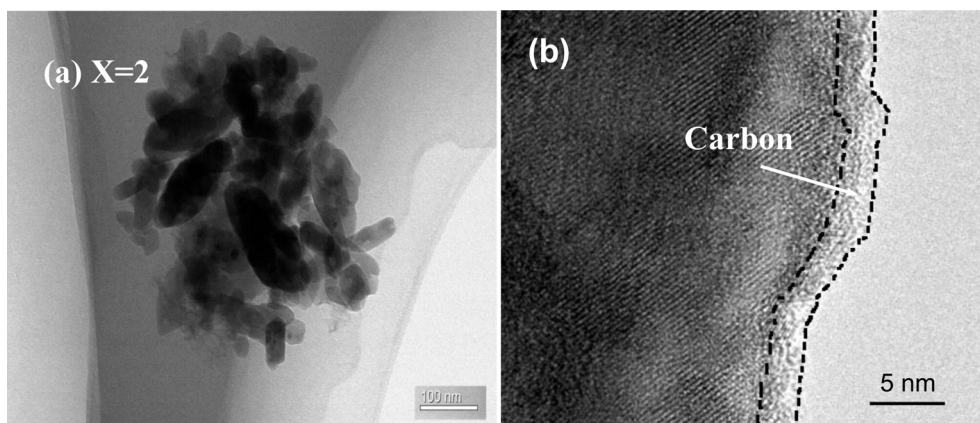

Fig. 3. (a–b) FE-HRTEM micrograph of $X = 2$ sample.

particles can be maintained even after calcination at 600 °C. The typical FE-HRTEM images of $X = 2$ sample are shown in Fig. 3. Fig. 3a clearly exhibits the irregular flaky shaped particles, and Fig. 3b shows a continuous and uniform carbon layer (~2 nm) along the LiMnPO$_4$ surface.

Fig. 4 shows the first charge–discharge profiles of the C-LMP samples. All the cells are charged at 0.05 C (8.5 mA g^{-1}) to 4.5 V, held at 4.5 V for 1.5 h, and discharged at 0.05 C to 2.5 V. A high and flat redox potential is observed around 4.1 V (vs. Li/Li$^+$), which is 0.6–0.7 V higher than that in LiFePO$_4$ cathodes [1,3,5]. All the samples prepared by the polyol-assistant hydrothermal method can deliver much higher capacities than that of the sample-BS (no polyol assisting), which indicates that the new synthesis method can greatly improve the electrochemical performance of LiMnPO$_4$. The gap 0.1409 V between charge and discharge plateaus for $X = 2$ sample is the narrowest one which suggests that $X = 2$ sample has the lowest overall resistance.

The discharge profiles of the C-LMP samples at 0.1 C (17 mA g^{-1}) are shown in Fig. 5. The $X = 2$ sample delivers a reversible capacity of 147.4 mA h g^{-1} which is the highest value ever reported [2,8,13,14,16–19]. The capacities for samples $X = 10$ and $X = 0.5$ are 136.2 mA h g^{-1} and 129.7 mA h g^{-1} respectively, and for Sample-BS is only 98.2 mA h g^{-1}. Compared with 74% capacity retention for sample-BS, the superior capacity retention for samples $X = 2$, $X = 10$ and $X = 0.5$ are all higher than 95% after 40 cycles. The perfect cyclic life shows the Jahn–Teller distortion [4,5] has little effect on the C/LMP samples prepared by the polyol-assisted hydrothermal method. The result makes a sharp contrast to the popular viewpoint that the large volume change from LiMnPO$_4$ to MnPO$_4$ caused by Jahn–Teller distortion will lead to rapid mechanical degradation of the electrode and worse cyclic life of the cells. We deem that the greatly improved performance can be attributed to the new synthesis method, which results in nanocrystalline LiMnPO$_4$ and a particular morphology to shorten Li$^+$ diffusion pathway.

The voltage profiles of $X = 2$ sample at various discharge rates are shown in Fig. S2, and its inset shows the typical charge–discharge profiles of $X = 2$ sample at C/5. Fig. 6 shows the specific discharge capacity of $X = 2$ sample in cycling at different rates varying from C/20 (8.5 mA g^{-1}) to 4 C (680 mA g^{-1}) between 2.5
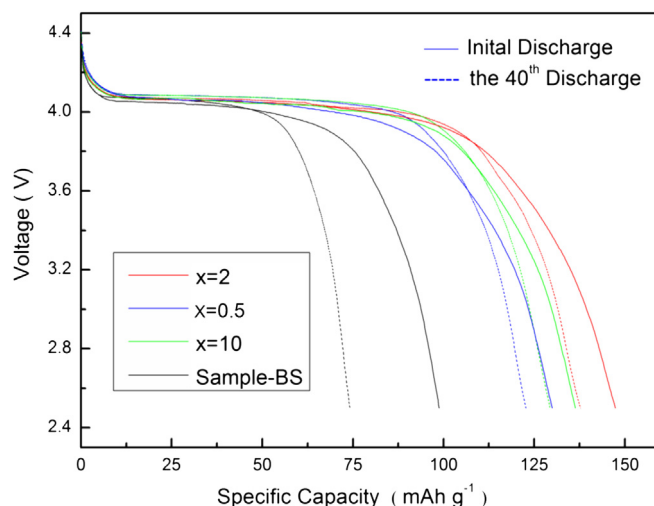

Fig. 5. Discharge curves of 1st and 40th at 0.1 C.

and 4.5 V, and the test at each rate sustains for 5 cycles. The excellent rate capability and the stable cyclic performance at different discharge rates are obtained. The discharge capacities decrease slightly from 154.1 mA h g^{-1} at C/20 to 147.4 mA h g^{-1} at C/10, 124.3 mA h g^{-1} at C/2 and 114.9 mA h g^{-1} at 1 C respectively. And the sample can still deliver ~69% of its initial capacity at 2 C rate, and 60% of that even at 4 C rate. The capacity loss accompanying increased rates is reversible, and a specific capacity of ~140 mA h g^{-1} can be recovered at 0.1 C after discharged at 4 C rate. The excellent rate performance of $X = 2$ sample indicates the Li$^+$ diffusion is fast and the intercalation/deintercalation processes is reversible. The rate capabilities of different C-LMP samples are compared in the inset. $X = 2$ sample shows the best rate capability, which can be attributed to its largest unit cell volume (303.22 Å^3) and the smaller crystallite size (33.46 nm). The larger lattice volume makes the Li$^+$ diffusion pathway much broader, and the smaller crystallite size shortens the Li$^+$ diffusion pathway, both of which can favor Li$^+$ mobility, resulting to a high rate performance.
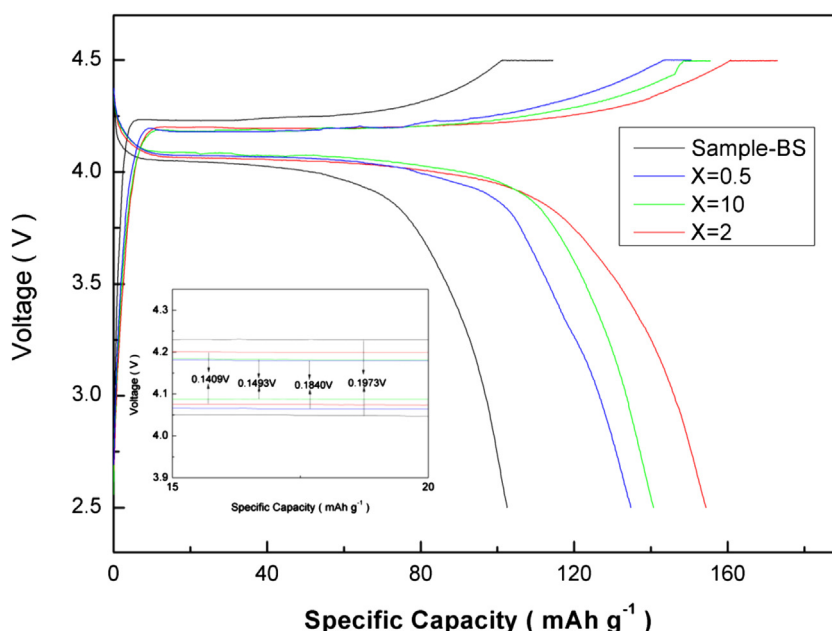

Fig. 4. Charge–discharge profiles of C-LMP samples at 0.05 C, inset: the gap between charge and discharge plateaus.
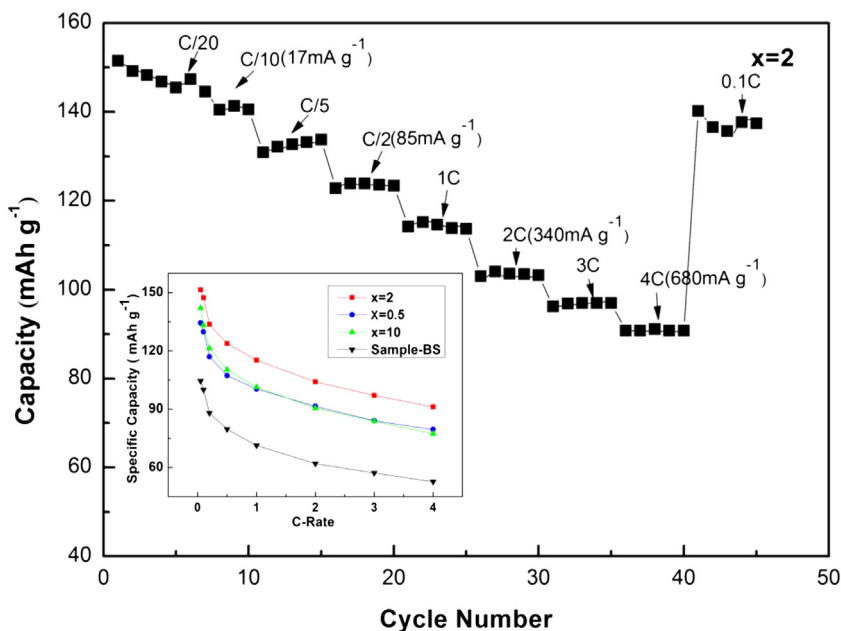
Fig. 6. The rate and cycling performance of $X = 2$ sample, insert: rate capacity retention.

The electrochemical impedance spectroscopy is measured at room temperature after 5th cycle (at 0.05 C with CC–CV mode). All EIS plots in Fig. 7 consist of a slightly depressed semicircle in the high-to-medium frequency region followed by a steep sloping line in the low frequency region. The semicircle corresponding to the charge transfer resistance is related to the interfacial Li^+ transfer, and the inclined line representing the Warburg impedance is responsible for the Li^+ diffusion in the $LiMnPO_4$ particles. The semicircle diameter for $X = 2$ sample is the smallest, and its Warburg slope is the biggest among all the samples. The impedance profile of the $X = 10$ sample is similar to that of $X = 2$ sample, but its semicircle diameter becomes much bigger after 40th cycle (Fig. S3), which indicates the charge transfer resistance of $X = 10$ sample increases more severely than that of $X = 2$ sample. All these could indicate the enhanced interfacial Li^+ transfer and greatly improved electrochemical kinetics of Li^+ extraction/insertion [5,13] in $X = 2$

sample, and the conclusion collaborates well with the above electrochemical test results. Altogether, the electrochemical properties of the synthesized C-LMP samples indicate that the polyol-assisted hydrothermal synthesis is a much more promising method to prepare the high-performance $LiMnPO_4$. However, the role of DEG at high-temperature and high-pressure hydrothermal condition is still unclear, and more efforts will be focused on this field in the future.

4. Conclusion

A delicate polyol-assisted hydrothermal method has been successfully applied to prepare high-performance $LiMnPO_4$ nanoparticles. Li_3PO_4 precursor with hollow sphere secondary structure was used to restrain the particle growth, and the water–DEG ratio was changed to control the particle morphology. The irregular flaky shaped $LiMnPO_4$ exhibits the best electrochemical performance, which can deliver a discharge capacity of 154.1 mA h g^{-1} at C/20, 147.4 mA h g^{-1} at C/10 and 102.5 mA h g^{-1} at 2 C respectively. The new synthesis method takes advantage of both the hydrothermal effect to produce nanocrystalline $LiMnPO_4$ and the polyol effect to influence the crystal growth orientation as a soft template, and it is highly suitable for all other $LiMPO_4$ olivine-type materials synthesis.

Appendix A. Supplementary data

Supplementary data related to this article can be found at http://dx.doi.org/10.1016/j.jpowsour.2013.10.036.

Fig. 7. Electrochemical impedance spectroscopy results of C-LMP composite cathodes after 5th cycle.

References

[1] A.K. Padhi, K.S. Nanjundaswamy, J.B. Goodenough, J. Electrochem. Soc. 144 (1997) 1188.

[2] X.-L. Pan, C.-Y. Xu, D. Honga, H.-T. Fang, L. Zhen, Electrochim. Acta 87 (2013) 303–308.
[3] Z.H. Chen, J.R. Dahn, J. Electrochem. Soc. 149 (2002) A1184–A1189.
[4] L. Chen, Y.-Q. Yuan, X. Feng, M.-W. Li, J. Power Sources 214 (2012) 344–350.
[5] C. Delacourt, L. Laffont, R. Bouchet, C. Wurm, J.-B. Leriche, M. Morcrette, J.-M. Tarascon, C. Masquelier, J. Electrochem. Soc. 152 (2005) A913–A921.
[6] S.-P. Ong, A. Jain, Ge. Hautier, B. Kang, G. Ceder, Electrochem. Commun. 12 (2010) 427–430.
[7] D. Choi, D.H. Wang, I.-T. Bae, J. Xiao, Z. Nie, W. Wang, V.V. Viswanathan, Y.J. Lee, J.-G. Zhang, G.L. Graff, Z.G. Yang, J. Liu, Nano Lett. 10 (2010) 2799–2805.
[8] T.-H. Kim, H.-S. Park, M.-H. Lee, S.-Y. Lee, H.-K. Song, J. Power Sources 172 (2007) 1–6.
[9] D. Wanga, H. Buqa, M. Crouzet, G. Deghenghi, T. Drezen, I. Exnar, N.-H. Kwon, J.H. Miners, L. Poletto, M. Grätzel, J. Power Sources 189 (2009) 624–628.
[10] Z. Bakenov, I. Taniguchil, Electrochem. Commun. 12 (2010) 75–78.
[11] J. Kim, K.-Y. Park, I. Park, J.-K. Yoo, D.-H. Seo, S.-W. Kim, Ki. Kang, J. Electrochem. Soc. 15 (2012) A55–A59.
[12] K. Dokko, T. Hachida, M. Watanabe, J. Electrochem. Soc. 158 (2011) A1275–A1281.
[13] Z. Bakenov, I. Taniguchi, J. Power Sources 195 (2010) 7445–7451.
[14] B.S.-M. Oh, S.-W. Oh, C.-S. Yoon, B. Scrosati, K. Amine, Y.-K. Sun, Adv. Funct. Mater. 20 (2010) 3260–3265.
[15] T. Shiratsuchi, S. Okada, T. Doi, J. Yamaki, Electrochim. Acta 54 (2009) 3145–3151.
[16] N.P.W. Pieczonka, Z.-Y. Liu, A. Huq, J.-H. Kim, J. Power Sources 230 (2013) 122–129.
[17] M. Pivko, M. Bele, E. Tchernychova, N.Z. Logar, R. Dominko, M. Gaberscek, Chem. Mater. 24 (2012) 1041–1047.
[18] J.-L. Liu, X.Y. Liu, T. Huang, A. Yu, J. Power Sources 229 (2013) 203–209.
[19] Y.-B. Cao, J.-G. Duan, G.-R. Hu, F. Jiang, Z.-D. Peng, K. Du, H.-W. Guo, Electrochim. Acta 98 (2013) 183–189.